Importance of Suppression of Yb^{3+} De-Excitation to Upconversion Enhancement in β-NaYF$_4$: Yb^{3+}/Er^{3+}@β-NaYF$_4$ Sandwiched Structure Nanocrystals

Guotao Xiang,[†,‡] Jiahua Zhang,*[,†] Zhendong Hao,[†] Xia Zhang,[†] Guo-Hui Pan,[†] Yongshi Luo,[†] Wei Lü,[§] and Haifeng Zhao[†]

[†]State Key Laboratory of Luminescence and Applications, Changchun Institute of Optics, Fine Mechanics and Physics, Chinese Academy of Sciences, 3888 Eastern South Lake Road, Changchun 130033, China

[‡]Graduate School of Chinese Academy of Sciences, Beijing 100039, China

[§]State Key Laboratory of Rare Earth Resource Utilization, Changchun Institute of Applied Chemistry, Chinese Academy of Sciences, Changchun 130022, China

Ⓢ *Supporting Information*

ABSTRACT: Nanosized Yb^{3+} and Er^{3+} co-doped β-NaYF$_4$ cores coated with multiple β-NaYF$_4$ shell layers were synthesized by a solvothermal process. X-ray diffraction and scanning electron microscopy were used to characterize the crystal structure and morphology of the materials. The visible and near-infrared spectra as well as the decay curves were also measured. A 40-fold intensity increase for the green upconversion and a 34-fold intensity increase for the red upconversion were observed as the cores are coated with three

shell layers. The origin of the upconversion enhancement was studied on the basis of photoluminescence spectra and decay times. Our results indicate that the upconversion enhancement in the sandwiched structure mainly originates from the suppression of de-excitation of Yb^{3+} ions. We also explored the population of the Er^{3+} ^{4}F$_{9/2}$ level. The results reveal that energy transfer from the lower intermediate Er^{3+} ^{4}I$_{13/2}$ level is dominant for populating the Er^{3+} ^{4}F$_{9/2}$ level when the nanocrystal size is relatively small; however, with increasing nanocrystal size, the contribution of the green emitting Er^{3+} ^{4}S$_{3/2}$ level for populating the Er^{3+} ^{4}F$_{9/2}$ level, which mainly comes from the cross relaxation energy transfer from Er^{3+} ions to Yb^{3+} ions followed by energy back transfer within the same Er^{3+}−Yb^{3+} pair, becomes more and more important. Moreover, this mechanism takes place only in the nearest Er^{3+}−Yb^{3+} pairs. This population route is in good agreement with that in nanomaterials and bulk materials.
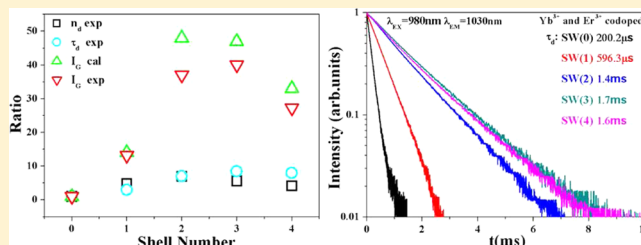
■ INTRODUCTION

For the past several years, trivalent rare earth ion doped fluoride upconversion (UC) nanocrystals (NCs) have attracted much attention.[1−4] UC NCs emit visible photons by absorbing two or more near-infrared (NIR) photons.[5] Thanks to such a unique luminescence mechanism, the UC nanoparticles can be applied to bioimaging, photodynamic therapy, UC lasers, photovoltaics, optical memory, and so on.[6−11] In comparison to conventional downconversion fluorescent materials such as organic dyes and quantum dots, UC NCs have obvious advantages, such as sharp emission bands, long emission lifetimes, higher photochemical stability, low toxicity, and little background autofluorescence.[12−17] However, the poor UC quantum yield is a serious problem.[18,19] This is certainly true for biological applications where excitation power is restricted, and the UC quantum yield is thus even an order of magnitude lower.[20] In recent years, large efforts have been devoted to improve UC quantum yield.[20−23] A core−shell structure is a promising approach to achieve the goal.[24−30]

Considerable studies have shown that rare earth doped β-NaYF$_4$ is acknowledged as the most efficient UC host material because of its low photon energy (360 cm^{-1}).[31−33] Meanwhile, large efforts have been devoted to the study of β-NaYF$_4$ core−shell structure in recent years.[24−30] Veggel et al. have reported the synthesis of β-NaYF$_4$/β-NaGdF$_4$ NC core−shell structure, and the quantum yield of Yb^{3+} and Er^{3+} co-doped NCs was increased from 0.1% to 0.3% by a core−shell structure.[1,19] In general, the UC enhancement by a core−shell structure in the Er^{3+}−Yb^{3+} system is roughly attributed to suppression of particle surface induced de-excitation of luminescent centers. However, the UC process involves interaction among various excited states; the degree of population increases of these states and their contributions to the UC enhancement in the presence of core−shell structure are rarely studied.

In this Article, β-NaYF$_4$:Yb^{3+}/Er^{3+} cores coated with different numbers of β-NaYF$_4$ shell layers were prepared. The prepared NCs are sandwiched structures, because they can function similarly to core−shell structures that can enhance the UC. A 40-fold intensity increase for the green UC and 34-fold
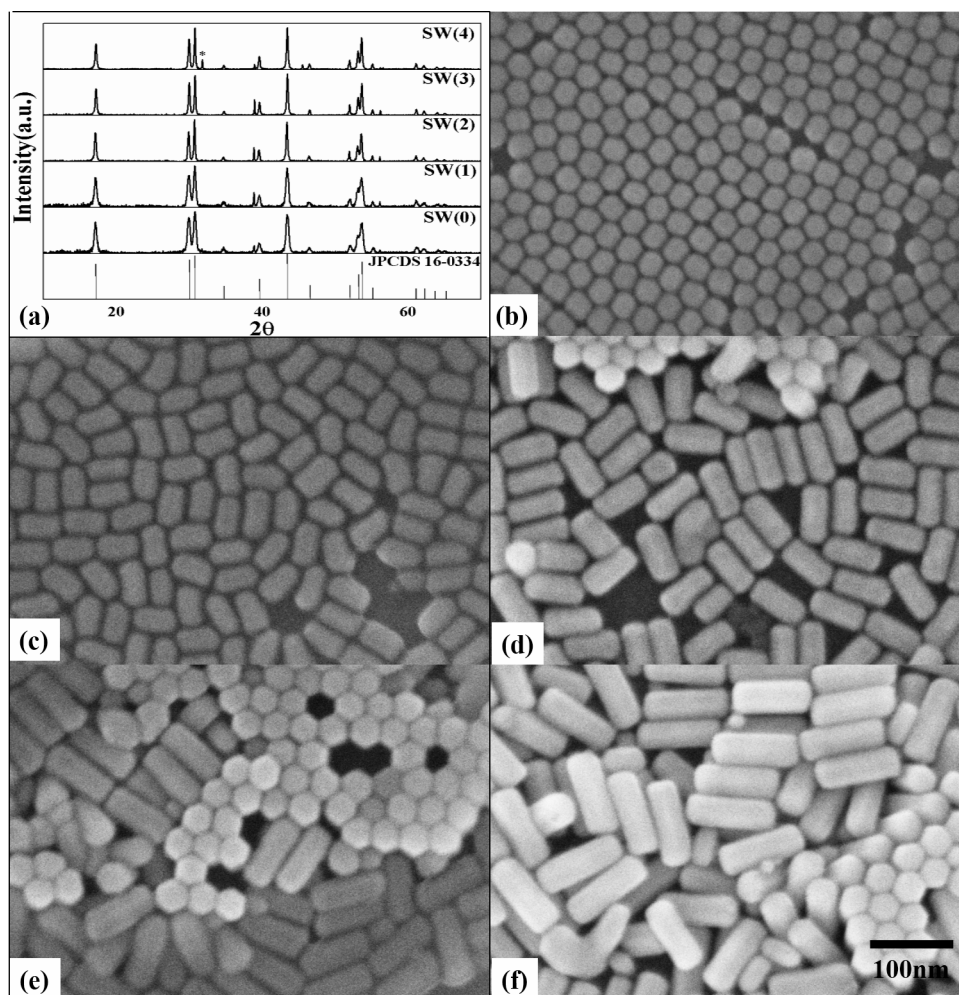
Figure 1. (a) Standard XRD data of β-NaYF$_4$ (JCPDS 16-0334) and the XRD patterns of the NaYF$_4$ sandwiched structure NCs with different shell numbers. The SEM images of the NaYF$_4$ sandwiched structure NCs with different shell numbers: (b) SW(0), (c) SW(1), (d) SW(2), (e) SW(3), and (f) SW(4).

intensity increase for the red UC were observed as three shell layers are coated. On the basis of the analysis of photoluminescence spectra and decay times, the UC enhancement is simulated, and the suppression of Yb^{3+} ion de-excitation by sandwiched structure is found to be the main mechanism for the UC enhancement. We also explored a new population route for the red emitting Er^{3+} $^4F_{9/2}$ level.

■ EXPERIMENTAL SECTION

Chemicals. NaOH, NH$_4$F, HCl, methanol, and ethanol were obtained from Beijing Chemical Reagent Company. Hexanes and oleic acid (OA) were obtained from Tianjin Guangfu Chemical Reagent Company. Lanthanide (Ln) oxides of SpecPure grade (Y$_2$O$_3$, Yb$_2$O$_3$, Er$_6$O$_{11}$, 99.99%) were purchased from the Yangkou state-run rare earth company. 1-Octadecene (ODE, 90%) was supplied by Alfa Aesar. All of the chemical reagents were used as received without further purification. LnCl$_3$ was prepared by dissolving the corresponding lanthanide oxides in hydrochloric acid.

Preparation of LnCl$_3$ (Ln = Y, Yb, Er) Precursors. In a typical synthesis, the corresponding lanthanide oxides of LnCl$_3$ were dissolved into dilute hydrochloric acid, resulting in the formation of a colorless solution of LnCl$_3$. After the solution was evaporated and then dried at 100 °C for 12 h in vacuum conditions, a powder of LnCl$_3$ was obtained.

Preparation of β-NaYF$_4$: 20% Yb^{3+}, 2% Er^{3+} Core (SW(0)) NCs. All of the doping ratios of Ln^{3+} are molar in our experiments. A

typical procedure for the synthesis of β-NaYF$_4$ 20% Yb^{3+}, 2% Er^{3+} core NCs follows: 1 mmol RECl$_3$ (RE = 0.78 Y, 0.2 Yb, 0.02 Er) were added to a 100 mL three-neck round-bottom flask containing ODE (15 mL) and OA (6 mL). The solution was magnetically stirred and heated to 140 °C for 30 min to form the lanthanide oleate complexes and remove residual water and oxygen. The temperature was then cooled to 50 °C with a gentle flow of argon gas through the reaction flask. Meanwhile, a solution of NH$_4$F (4 mmol) and NaOH (2.5 mmol) dissolved in methanol (10 mL) was added to the flask, and the resulting mixture was stirred for 30 min to evaporate methanol from the reaction mixture. The temperature was then increased to 300 °C in an argon atmosphere for 90 min and then naturally cooled to room temperature. The resultant solid state products were precipitated by the addition of ethanol, collected by centrifugation, washed with ethanol three times, and finally redispersed in cyclohexane.

Preparation of β-NaYF$_4$ Sandwiched Structure NCs with Different Numbers of β-NaYF$_4$ Shell Layers. For the synthesis of SW(x) NCs (x = 1−4), 1 mmol of YCl$_3$ was added to a 100 mL three-neck round-bottom flask containing ODE (15 mL) and OA (6 mL). The solution was magnetically stirred and heated to 140 °C for 30 min to form the lanthanide oleate complexes and remove residual water and oxygen. The temperature was lowered to 80 °C and the reaction flask placed under a gentle flow of argon. A solution of 1 mmol SW(x − 1) NCs in 10−15 mL of hexanes was added to the solution. The solution was maintained at 80 °C until all the hexanes were removed. The reaction mixture was cooled to 50 °C with a gentle flow of argon gas through the reaction flask. Meanwhile, a solution of NH$_4$F (4

mmol) and NaOH (2.5 mmol) dissolved in methanol (10 mL) was added to the flask, and the resulting mixture was stirred for 30 min to evaporate methanol from the reaction mixture. The temperature was then raised to 300 °C in an argon atmosphere for 90 min and then naturally cooled to room temperature. The resultant solid state products were precipitated by the addition of ethanol, collected by centrifugation, washed with ethanol three times, and finally redispersed in cyclohexane.

Characterization. Powder X-ray diffraction (XRD) data were collected using Cu Kα radiation (λ = 1.540 56 Å) on a Bruker D8 advance diffractometer equipped with a linear position-sensitive detector (PSD-50 m, M.Braun), operating at 40 kV and 40 mA with a step size of 0.01° (2θ) in the range 10°−70°. The morphology was investigated by field emission scanning electron microscopy (SEM) (Hitachi S-4800). The chemical analysis of samples was inspected on a field emission scanning electron microscope (SEM, Hitachi S-4800) equipped with an energy dispersive X-ray spectrum (EDS, JEOL JXA-840). The UC spectra were measured using an FLS920 spectrometer (Edinburgh Instruments, U.K.) pumped with a power-controllable 980 nm diode laser. The emission spectrum under direct excitation was measured using an FLS920 spectrometer (Edinburgh Instruments, U.K.). In fluorescence lifetime measurements, an optical parametric oscillator (OPO) was used as an excitation source, and the signals were detected by a Tektronix digital oscilloscope (TDS 3052). The lifetimes were calculated via integration of the area under the corresponding decay curves with the normalized initial intensity.

■ RESULTS AND DISCUSSION

Structure and Morphology. The crystal structures and the phase purity of the as-prepared products were examined by XRD, as shown in Figure 1a. The positions and relative intensities of the XRD peaks can be indexed well to the standard cards of β-NaYF$_4$ (JCPDS 16-0334). No second phase is detected except the diffraction peaks of NaCl, which are represented by the asterisks. SEM was used to evaluate the morphology of the prepared NCs. Figure 1b−f shows the SEM images of the final products with different shell numbers: (b) SW(0), (c) SW(1), (d) SW(2), (e) SW(3), and (f) SW(4). The bare β-NaYF$_4$ cores present hexagonal nanosheets with a diameter of 30 nm (see Figure 1b), and these NCs have good monodispersity. After growing a shell or shells on the cores, the sandwiched structure NCs present hexagonal nanorods with the same diameter of 30 nm and different lengths. Supporting Information Figure S1 depicts the histograms of the length distribution of SW(1), SW(2), SW(3), and SW(4); these data were obtained from the SEM images of more than 100 corresponding NCs. As illustrated in Supporting Information Figure S1, the average lengths of SW(1), SW(2), SW(3), and SW(4) are 50, 70, 90, and 110 nm, respectively. From this, we can conclude that the shells grow along the core NC axes in the vertical direction, and the growth of other directions is limited. Beyond that, the thickness of each individual shell is about 20 nm. Further, the EDS of SW(0) and SW(3) was measured to prove the sandwiched structures (see Supporting Information Figure S2). In comparison with that of SW(0), the peak for Yb was not observed in SW(3), suggesting that the Yb^{3+} species were doped in the NCs, not on the surface. Therefore, it shows that the prepared NCs are indeed sandwiched structures. In addition, due to the lower concentration of Er^{3+} (2 mol %), it is difficult to detect the peak for Er.

Enhancement of UC. Figure 2 shows the UC emission spectra of the resulting NCs pumped by a 980 nm diode laser with output power density of 3 mW/mm^2. The green emissions in the range 510−570 nm are assigned to the ^{2}H$_{11/2}$ → ^{4}I$_{15/2}$ and ^{4}S$_{3/2}$ → ^{4}I$_{15/2}$ transitions of Er^{3+}. The red emission in the
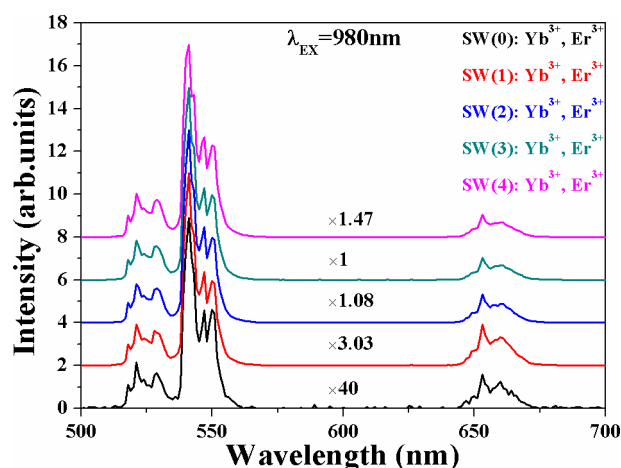

Figure 2. UC spectra of the resulting NCs under 980 nm excitation with a low pump density of 3 mW/mm^2. Spectra are normalized to the maximum intensity of ^{4}S$_{3/2}$ → ^{4}I$_{15/2}$ transition.

range 640−683 nm is assigned to the ^{4}F$_{9/2}$ → ^{4}I$_{15/2}$ transition of Er^{3+}. It is noticed that the UC emission intensity is strongly enhanced as the shell numbers increase up to three. The green emission and the red emission are enhanced by factors of 40 and 34, respectively, for shell layer number of three. The decrease in the UC emission intensity for shell number of four can be explained as the reduction of core number per volume with increasing the shell thickness. More specifically, for shell number of four, the amounts of Yb^{3+} ions and Er^{3+} ions per volume decrease with the increase in the NC's size; moreover, all the measurement conditions are the same during the measurement process, so one can be sure that the amount of the NIR photon radiating on the measurement samples in equal times as well as the absorbing area of the measurement samples are the same. Thus, the NIR photon absorbed by the samples at equal times would decrease with the increase in the NC size, which results in the decrease of the UC emission intensity of SW(4). The UC enhancement in sandwiched structure NCs is generally attributed to surface modification induced reduction of luminescence quenchers on the surface of the cores. In energy transfer upconversion (ETU) of the Er^{3+}−Yb^{3+} system (see Figure 3), the intensity of the green UC is proportional to the population of the ^{2}F$_{5/2}$ level of Yb^{3+} (n_d), the population of the ^{4}I$_{11/2}$ level of Er^{3+} (n_2), and the emission efficiency of the green emitting state (η_G). Therefore, for a single NC, the intensity of the green UC can be expressed as

$$I_{\text{UCG}} = C_{d5}\eta_G n_2{}'n_d{}' \tag{1}$$

Here C_{d5} is the coefficient for energy transfer (ET) from excited Yb^{3+} to Er^{3+} in the ^{4}I$_{11/2}$ state to promote excitation of the ^{4}F$_{7/2}$ level of Er^{3+}, $n_2{}'$ is the population of the ^{4}I$_{11/2}$ level of Er^{3+} for a single NC, and $n_d{}'$ is the population of the ^{2}F$_{5/2}$ level of Yb^{3+} for a single NC. If C_{d5} is independent of the sandwiched structure, the UC enhancement refers to the enhancement of $\eta_G n_2{}'n_d{}'$ by the sandwiched structure. What we are interested in is examination of the consistency of the green UC intensity with $\eta_G n_2{}'n_d{}'$ that can be obtained from downconversion luminescence spectra. On the basis of this study, we may know which one of the populations ($n_2{}'$, $n_d{}'$) and its emission efficiency η_G are more sensitive to sandwiched structure.

On the basis of eq 1, with the assumption that there are m cores in the 980 nm irradiation area, then the emission intensity of the green UC from each core is
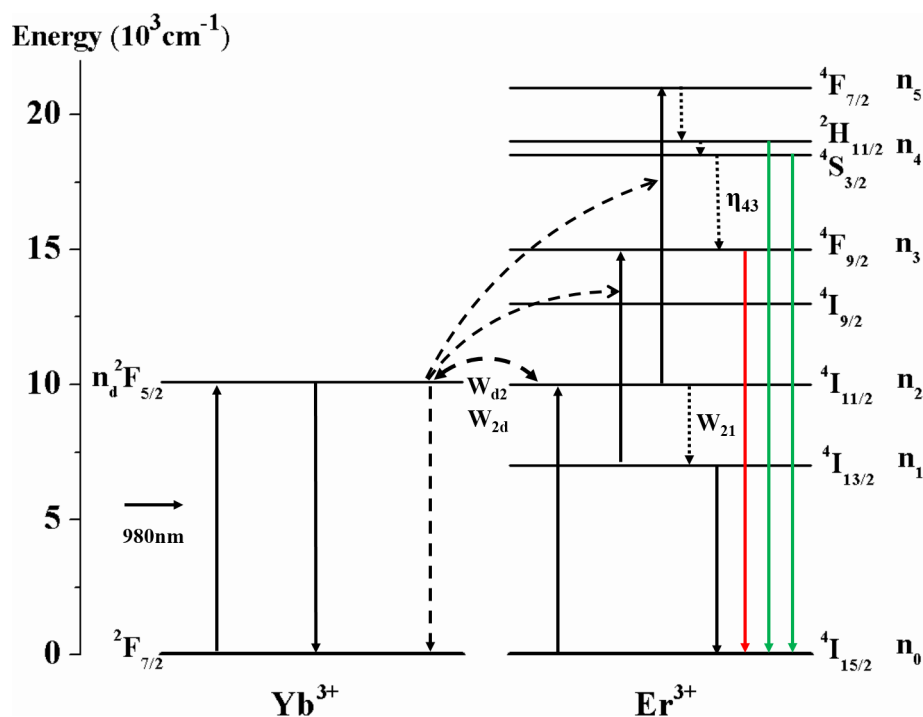
Figure 3. Energy level diagrams and various mainly ET mechanisms in Yb^{3+} and Er^{3+} co-doped β-NaYF$_4$ sandwiched structure NCs following 980 nm excitation.

$$I_g = C_{ds}\eta_G(n_2/m)(n_d/m) = C_{ds}\eta_G n_2 n_d/m^2 \tag{2}$$

For the total emission intensity of the green UC is

$$I_G = mC_{ds}\eta_G n_2 n_d/m^2 = C_{ds}\eta_G n_2 n_d/m \tag{3}$$

If the number of the infrared photons absorbed by each core per time is p, then

$$mp = n_d/\tau_d \tag{4}$$

Here τ_d is the decay time of the $Yb^{3+2}F_{5/2}$ level. With eq 4, eq 3 can be written as

$$I_G = pC_{ds}\eta_G n_2\tau_d \tag{5}$$

For Yb^{3+} ion and Er^{3+} ion co-doped samples, the NIR emission of $Er^{3+4}I_{11/2}$ level is hidden by the NIR emission of the $Yb^{3+2}F_{5/2}$ level, which suggests that determination of n_2 agreement is difficult. In order to explore the properties of the $Er^{3+4}I_{11/2}$ level, we measured the NIR spectra excited by 808 and 980 nm wavelengths, respectively. The NIR spectra are shown in Figure 4, and the intensities of the $^4I_{13/2} \rightarrow {}^4I_{15/2}$ transition are normalized to 1. As shown in Figure 4, the ratio of the $^2F_{5/2} \rightarrow {}^2F_{7/2}$ transition to the $^4I_{13/2} \rightarrow {}^4I_{15/2}$ transition excited by the 808 nm wavelength is very similar to that excited by the 980 nm wavelength for the same sample. Before we explain this phenomenon, it is worth noting that the $Er^{3+4}I_{9/2}$ level is excited directly under 808 nm excitation and the $Yb^{3+2}F_{5/2}$ level is excited directly under 980 nm excitation. That is to say, whether the $Er^{3+4}I_{9/2}$ level or the $Yb^{3+2}F_{5/2}$ level is excited, the ratio of $^2F_{5/2} \rightarrow {}^2F_{7/2}$ transition to $^4I_{13/2} \rightarrow {}^4I_{15/2}$ transition stays unchanged for the same sample. This indicates that the $Er^{3+4}I_{11/2}$ level and the $Yb^{3+2}F_{5/2}$ level are thermally and rapidly coupled in the case of fast ET between them due to high concentration of Yb^{3+} ions, as predicted earlier.[34] Hence, the population ratio of the two levels stays unchanged regardless of whether Yb^{3+} ions or Er^{3+} ions are directly excited. In view of
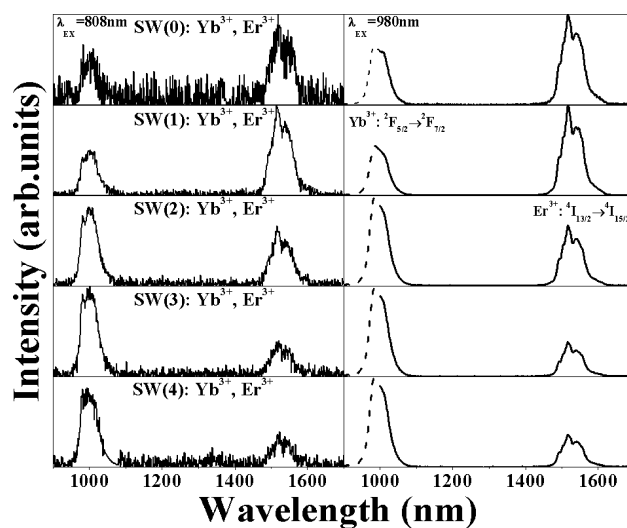

Figure 4. NIR spectra in Yb^{3+} and Er^{3+} co-doped β-NaYF$_4$ sandwiched structure NCs under 808 and 980 nm excitation, respectively. The intensities of $^4I_{13/2} \rightarrow {}^4I_{15/2}$ transition are normalized to 1.

the unchanged $^4I_{11/2} - {}^4I_{13/2}$ multiphonon relaxation rate with excitation wavelengths, the emission intensity ratio of the $^2F_{5/2} \rightarrow {}^2F_{7/2}$ transition to the $^4I_{13/2} \rightarrow {}^4I_{15/2}$ transition thus stays unchanged. Below we derived the population relationship between the $Yb^{3+2}F_{5/2}$ level and the $Er^{3+4}I_{11/2}$ level. The steady state equation of the $Yb^{3+2}F_{5/2}$ level under 808 nm excitation can be written as follows:

$$n_2W_{2d} = (W_{d2} + 1/\tau_d)n_d \tag{6}$$

Here W_{2d} is the ET rate from the $Er^{3+4}I_{11/2}$ level to the $Yb^{3+2}F_{5/2}$ level, and W_{d2} is the energy back transfer rate from the $Yb^{3+2}F_{5/2}$ level to the $Er^{3+4}I_{11/2}$ level. Considering W_{2d} and
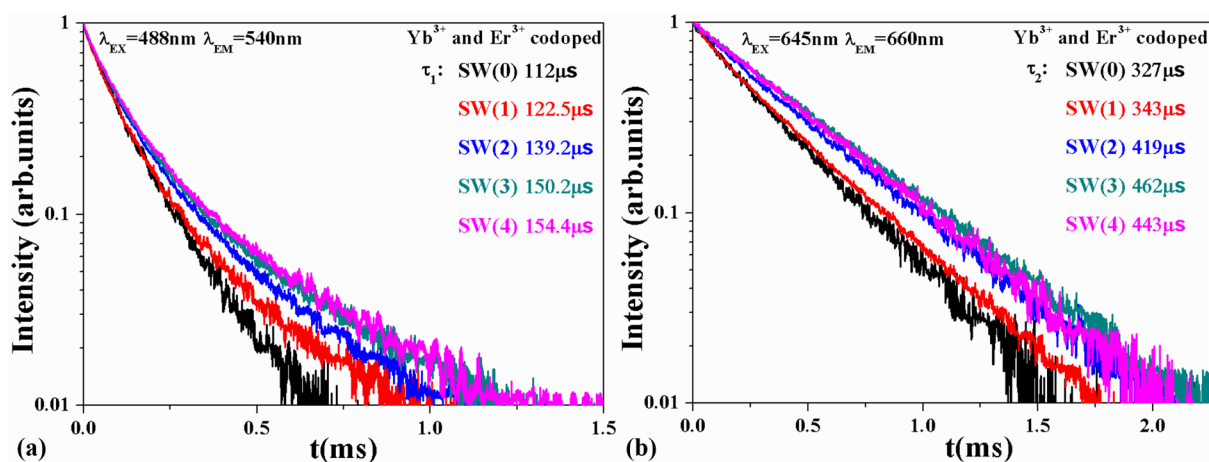
Figure 5. Lifetimes for (a) the $^4S_{3/2} \rightarrow {}^4I_{15/2}$ transition under 488 nm excitation wavelength and (b) the $^4F_{9/2} \rightarrow {}^4I_{15/2}$ transition under 645 nm excitation wavelength in Yb^{3+} and Er^{3+} co-doped β-$NaYF_4$ sandwiched structure NCs.

W_{d2} only depend on the doping concentration of Yb^{3+} ions and Er^{3+} ions and $W_{d2} \gg 1/\tau_d$, eq 5 can be written as

$$I_G = (pC_{d5}W_{d2}/W_{2d})\eta_G n_d \tau_d \qquad (7)$$

The lifetimes of the $Er^{3+4}S_{3/2}$ level under 488 nm excitation and the decay times of the $Yb^{3+2}F_{5/2}$ level under 980 nm excitation were measured and shown in Figures 5a and 6,
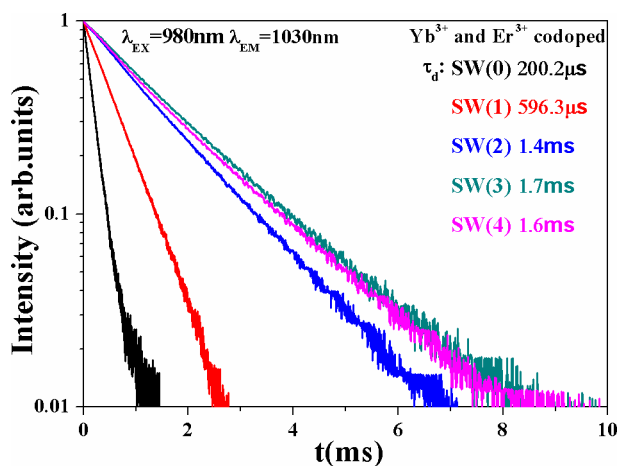

Figure 6. Decay curves for the $^2F_{5/2} \rightarrow {}^2F_{7/2}$ transition of Yb^{3+} ions under 980 nm excitation wavelength in the Yb^{3+} and Er^{3+} co-doped β-$NaYF_4$ sandwiched structure NCs.

respectively. As the lifetimes of the $Er^{3+4}S_{3/2}$ level show a small increase change, we ignored the change of the lifetimes of the $Er^{3+4}S_{3/2}$ level. Since the emission efficiency is proportional to the lifetime of the corresponding level, the changes of the values of η_G are ignored. Utilizing the foregoing data and eq 7, we can calculate the enhancement factor of UC. Figure 7 is the discrete map of the enhancement factors, including the experiment values and calculated values. As the calculated values are similar to the experiment values, this proves the legitimacy of our calculation formula deduced process.

Next, we will explore which is the determining factor in the UC enhancement for the sandwiched structure. Through a combination of eqs 4 and 7, then

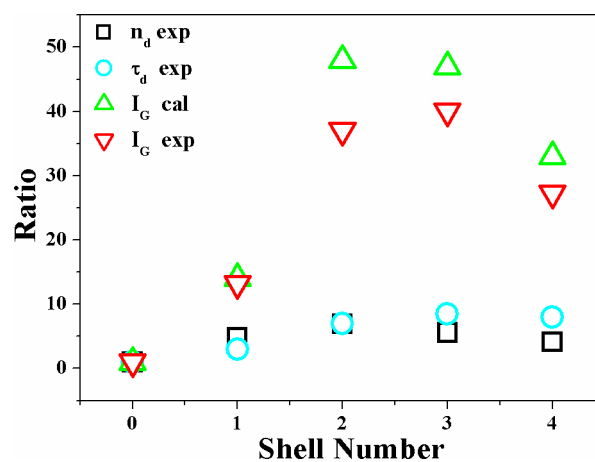$$I_G = m(p^2 C_{d5}W_{d2}/W_{2d})\eta_G \tau_d^2 \qquad (8)$$

Figure 7. Discrete map of n_d, τ_d, and the enhancement factors including the experiment values and calculated values. All of the values of SW(0) are normalized to 1.

If the values of m stay consistent

$$I_G \propto \eta_G \tau_d^2 \qquad (9)$$

Since the change of the values of η_G are ignored, the values of I_G mainly depend on τ_d. That is to say, the prolongation of the decay times of Yb^{3+} (τ_d) with the increase of the shell numbers is the determining factor in the UC enhancement for the sandwiched structure. As can be seen from Figure 6, the decay times of Yb^{3+} (τ_d) of the NCs with different shell numbers increase obviously as compared with those of SW(0). Moreover, for SW(3) and SW(4), the decay times of Yb^{3+} are very close to the intrinsic lifetime of Yb^{3+} in bulk materials, demonstrating the good performance of the sandwiched structure in UC enhancement.[35] The obvious increase of τ_d is due to the decrease of ET from the $Yb^{3+2}F_{5/2}$ level to the particles' surface resulting from the sandwiched structure. The high concentration of Yb^{3+} ions (20 mol % in our case) is considered as the main factor for explaining this phenomenon. The energy migration among Yb^{3+} ions is very fast due to the high Yb^{3+} ion concentration. Therefore, Yb^{3+} ions can transfer their energy to the defects and the solvent molecules on the particles' surface easily for SW(0). However, for a sandwiched structure, the amount of the defects and the solvent molecules on the particles' surfaces are reduced significantly, which results
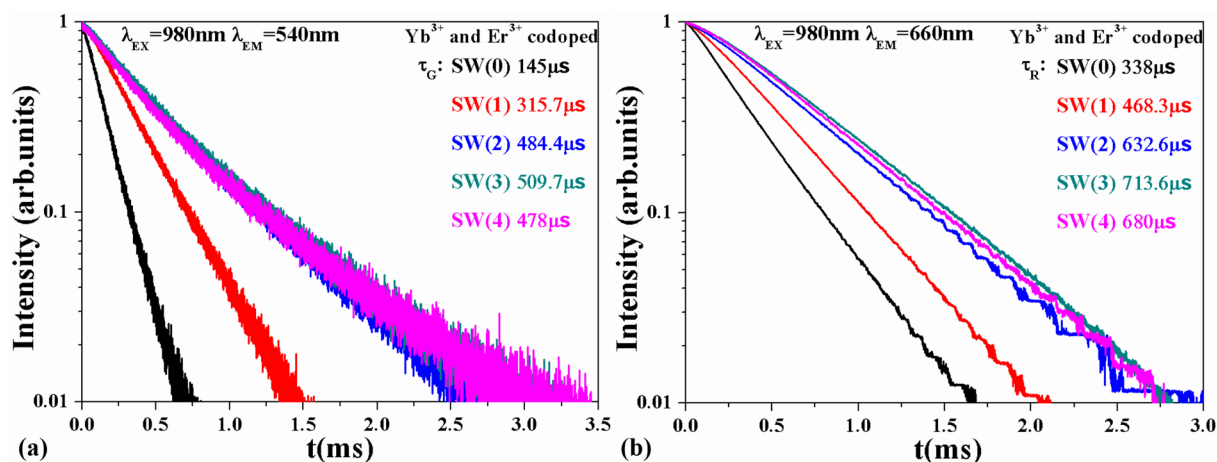
Figure 8. Decay curves for (a) $^4S_{3/2} \rightarrow {}^4I_{15/2}$ transition and (b) $^4F_{9/2} \rightarrow {}^4I_{15/2}$ transition under 980 nm wavelength excitation in Yb^{3+} and Er^{3+} co-doped β-NaYF$_4$ sandwiched structure NCs.

in the obvious reduction of ET process from $Yb^{3+2}F_{5/2}$ level to the particles' surfaces.

Population of the $^4F_{9/2}$ Level of Er^{3+}. At low 980 nm excitation densities, ET from the lower intermediate $Er^{3+4}I_{13/2}$ state and multiphonon relaxation (MPR) from the upper $Er^{3+4}S_{3/2}$ state are generally considered dominant for the population of the $Er^{3+4}F_{9/2}$ level in the Yb^{3+} and Er^{3+} co-doped system. In fact, at high concentration of Yb^{3+} ions (20 mol % in our case), a non-MPR mechanism for populating the $Er^{3+4}F_{9/2}$ level from the $Er^{3+4}S_{3/2}$ level occurs and was proposed earlier.[36] The ET involved in this mechanism takes place only in the nearest $Er^{3+}–Yb^{3+}$ pairs, and thus, it is fast and efficient at low excitation densities. The mechanism involves a cross relaxation (CR) ET from Er^{3+} in the $^4S_{3/2}$ excited state ($^4S_{3/2} \rightarrow {}^4I_{13/2}$) to Yb^{3+} in the ground state ($^2F_{7/2} \rightarrow {}^2F_{5/2}$) followed by an energy back transfer (CRB), taking place within the same $Er^{3+}–Yb^{3+}$ pair from the excited Yb^{3+} ($^2F_{5/2} \rightarrow {}^2F_{7/2}$) back to the original Er^{3+} in the $^4I_{13/2}$ excited state ($^4I_{13/2} \rightarrow {}^4F_{9/2}$), leading to the excitation of the $Er^{3+4}F_{9/2}$ level.[37,38]

First, we utilized the decay curves of the $Er^{3+4}S_{3/2}$ and $Er^{3+4}F_{9/2}$ levels excited by 980 nm wavelength excitation to prove that ETs from the lower intermediate $Er^{3+4}I_{13/2}$ state and the green emitting $Er^{3+4}S_{3/2}$ level both contribute to the population of the $Er^{3+4}F_{9/2}$ level. The decay curves of the $Er^{3+4}S_{3/2}$ level and the $Er^{3+4}F_{9/2}$ level excited by 980 nm wavelength are shown in Figure 8. For SW(2), SW(3), and SW(4), with the assumption that ET from the lower intermediate $Er^{3+4}I_{13/2}$ state is the main approach for the population of the $Er^{3+4}F_{9/2}$ level, then the decay times of the $Er^{3+4}F_{9/2}$ level are determined by the $Yb^{3+2}F_{5/2}$ and $Er^{3+4}I_{13/2}$ levels. Given that the decay times of the $Er^{3+4}I_{13/2}$ level are much longer than those of the $Yb^{3+2}F_{5/2}$ level and the decay times of the $Yb^{3+2}F_{5/2}$ level are much longer than the lifetimes of the $Er^{3+4}F_{9/2}$ level (see Figure 5b), the decay times of the $Er^{3+4}F_{9/2}$ level should be almost equal to the decay times of the $Yb^{3+2}F_{5/2}$ level.[23] With the assumption that the contribution of the green emitting state $Er^{3+4}S_{3/2}$ is dominant for the population of $Er^{3+4}F_{9/2}$ level, (1) for MPR process, the decay times of the $Er^{3+4}F_{9/2}$ level should be almost equal to the decay times of the $Er^{3+4}S_{3/2}$ level; (2) for CRB process, as the ET process between the nearest $Er^{3+}–Yb^{3+}$ pairs is fast, the decay times of the $Er^{3+4}F_{9/2}$ level should be also approximately equal to the corresponding decay times of the $Er^{3+4}S_{3/2}$ level. All in all, if the population of the $Er^{3+4}F_{9/2}$ level is mainly from the

green emitting $Er^{3+4}S_{3/2}$ level, the decay times of the $Er^{3+4}F_{9/2}$ level should be almost equal to the decay times of the $Er^{3+4}S_{3/2}$ level. With reference to the testing data, the decay times of the $Er^{3+4}F_{9/2}$ level are between their corresponding decay times of the $Er^{3+4}S_{3/2}$ level and the $Yb^{3+2}F_{5/2}$ level. So one can conclude that the populations of the $Er^{3+4}F_{9/2}$ level in SW(2), SW(3), and SW(4) originate from two processes: ET from the lower intermediate state $Er^{3+4}I_{13/2}$ level and contribution of the green emitting state $Er^{3+4}S_{3/2}$ level. In addition, as the two processes are irrelevant to the sandwiched structure, we suggest that they also exist in SW(0) and SW(1).

Next, in order to prove the existence of the CRB process, the photoluminescence (PL) spectrum excited by 488 nm wavelength light was measured and shown in Figure 9. In the
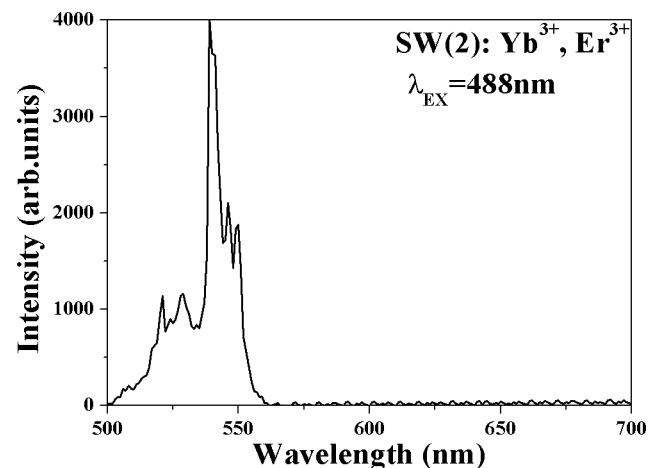

Figure 9. PL spectrum in Yb^{3+} and Er^{3+} co-doped SW(2) NCs under 488 nm excitation.

PL measurement, 488 nm is selected to excite the $Er^{3+4}F_{7/2}$ level, from which the excitation subsequently relaxes down to $Er^{3+2}H_{11/2}/{}^4S_{3/2}$ levels. In the range from 500 to 700 nm, the red emission of the $Er^{3+4}F_{9/2}$ level disappears compared with the corresponding UC spectrum. This result demonstrates that the MPR process and the CRB process are all inefficient for the population of the $Er^{3+4}F_{9/2}$ level under 488 nm excitation. However, we have proven that the population of the $Er^{3+4}F_{9/2}$ level partly originates from the green emitting state $Er^{3+4}S_{3/2}$

under 980 nm excitation. As the MPR process is not influenced by excitation wavelength, the contribution of the green emitting $Er^{3+4}S_{3/2}$ level for the population of the $Er^{3+4}F_{9/2}$ level under 980 nm excitation mainly comes from the CRB process. Besides, it should be noted that the CRB process under 488 nm excitation is much less efficient than that under 980 nm excitation. This is because all of the Er^{3+} ions in the NCs are excited under 488 nm excitation. However, the Er^{3+} ions far away from the Yb^{3+} ions are useless for the CRB process. Instead, under 980 nm wavelength light, only the Er^{3+} ions close to Yb^{3+} ions are excited, and they can take part in the CRB process. Therefore, under 488 nm excitation, the CRB process is very inefficient, showing that the red emission of the $Er^{3+4}F_{9/2}$ level is very weak.

To illustrate further the population of the $Er^{3+4}F_{9/2}$ level, we utilized the following steady state equation:

$$I_R = C_{d3}n_1n_d\eta_R + \eta_{43}I_G\eta_R \tag{10}$$

Here I_R is the intensity of $^4F_{9/2}$ level, C_{d3} is the coefficient for ET from excited Yb^{3+} ions to Er^{3+} ions in the $^4I_{13/2}$ state to promote excitation of $^4F_{9/2}$ level of Er^{3+}, n_1 is the population of $^4I_{13/2}$ level, η_R is the emission efficiency of $^4F_{9/2}$ level of Er^{3+}, and η_{43} is the transfer efficiency from the $Er^{3+4}S_{3/2}$ level to the $Er^{3+4}F_{9/2}$ level, which is independent of the sandwiched structure. When eq 10 is simplified

$$I_R/(I_G\eta_R) = \eta_{43} + C_{d3}n_1n_d/I_G \tag{11}$$

According to eq 11, we plotted the values of $I_R/(I_G\eta_R)$ as a function of the values of n_1n_d/I_G shown in Figure 10. The
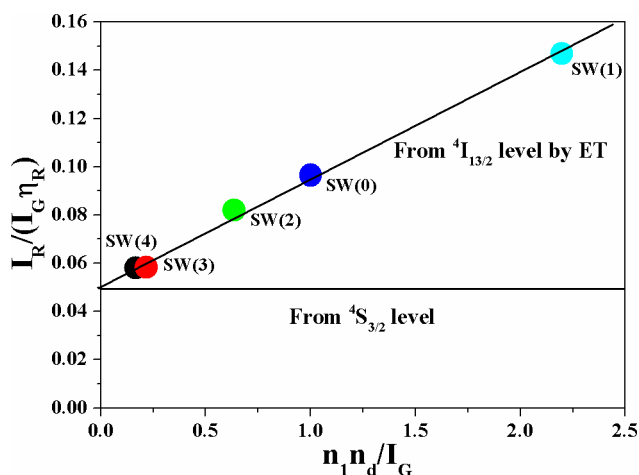
Figure 10. Values of $I_R/(I_G\eta_R)$ as a function of the values of n_1n_d/I_G.

discrete points are almost collinear. From Figure 10, we can see that the proportion of the contribution of the green emitting state $Er^{3+4}S_{3/2}$ level for populating the $Er^{3+4}F_{9/2}$ level increases with the increasing shell numbers. Also, if the shell numbers reach a critical value, then $n_1 = 0$, and the population of the $Er^{3+4}F_{9/2}$ level would all originate from the $Er^{3+4}S_{3/2}$ level. In other words, ET from the lower intermediate $Er^{3+4}I_{13/2}$ state is dominant for populating the $Er^{3+4}F_{9/2}$ level when the NC's size is relatively small; however, with increasing NC size, the green emitting $Er^{3+4}S_{3/2}$ level for populating the $Er^{3+4}F_{9/2}$ level becomes more and more important. This population route is in good agreement with that in nanomaterials and bulk materials.

CONCLUSIONS

In summary, we synthesized the $NaYF_4$ sandwiched structure NCs, and the enhancement of the UC intensity is very significant. Through analyzing photoluminescence spectra and decay times, we propose that the enhancement of the UC intensity mainly results from the suppression of de-excitation of Yb^{3+} ions, showing the increase of the decay times of the $Yb^{3+2}F_{5/2}$ level. We also explored the population of the $Er^{3+4}F_{9/2}$ level. The results reveal that ET from the lower intermediate $Er^{3+4}I_{13/2}$ state is dominant for populating the $Er^{3+4}F_{9/2}$ level when the NC size is relatively small; however, with the increasing NC size, the contribution from the green emitting $Er^{3+4}S_{3/2}$ level for populating the $Er^{3+4}F_{9/2}$ level, which mainly comes from the CRB process, becomes more and more important. This population route is in good agreement with that in nanomaterials and bulk materials.

ASSOCIATED CONTENT

S Supporting Information

Histograms of the length distribution and EDS spectra. This material is available free of charge via the Internet at http://pubs.acs.org.

AUTHOR INFORMATION

Corresponding Author

*E-mail: zhangjh@ciomp.ac.cn.

Notes

The authors declare no competing financial interest.

ACKNOWLEDGMENTS

REFERENCES

(1) Abel, K. A.; Boyer, J. C.; van Veggel, F. C. J. M. *J. Am. Chem. Soc.* **2009**, *131*, 14644−14645.

(2) Mai, H. X.; Zhang, Y. W.; Si, R.; Yan, Z. G.; Sun, L. D.; You, L. P.; Yan, C. H. *J. Am. Chem. Soc.* **2006**, *128*, 6426−6436.

(3) Teng, X.; Zhu, Y. H.; Wei, W.; Wang, S. C.; Huang, J. F.; Naccache, R.; Hu, W. B.; Tok, A. I. Y.; Han, Y.; Zhang, Q. C.; Fan, Q. L.; Huang, W.; Capobianco, J. A.; Huang, L. *J. Am. Chem. Soc.* **2012**, *134*, 8340−8343.

(4) Qin, W. P.; Liu, Z. Y.; Sin, C. N.; Wu, C. F.; Qin, G. S.; Chen, Z.; Zheng, K. Z. *Light: Sci. Appl.* **2014**, *3*, e193.

(5) Auzel, F. *Chem. Rev.* **2004**, *104*, 139−173.

(6) Wu, Z. N.; Guo, C. R.; Liang, S.; Zhang, H.; Wang, L. P.; Sun, H. C.; Yang, B. *J. Mater. Chem.* **2012**, *22*, 18596−18602.

(7) Jiang, G. C.; Pichaandi, J.; Johnson, N. J. J.; Burke, R. D.; van Veggel, F. C. J. M. *Langmuir* **2012**, *28*, 3239−3247.

(8) Chatterjee, D. K.; Gnanasammandhan, M. K.; Zhang, Y. *Small* **2010**, *24*, 2781−2795.

(9) Wang, G. F.; Peng, Q.; Li, Y. D. *Acc. Chem. Res.* **2011**, *44*, 322−332.

(10) Cui, S. S.; Chen, H. Y.; Zhu, H. Y.; Tian, J. M.; Chi, X. M.; Qian, Z. Y.; Achilefuc, S.; Gu, Y. Q. *J. Mater. Chem.* **2012**, *22*, 4861−4873.

(11) Dianov, E. M. *Light: Sci. Appl.* **2012**, *1*, e12.

(12) Jalil, R. A.; Zhang, Y. *Biomaterials* **2008**, *29*, 4122−4128.

(13) Wang, Z. L.; Hao, J. H.; Chan, H. L. W.; Law, G. L.; Wong, W. T.; Wong, K. L.; Murphy, M. B.; Su, T.; Zhang, Z. H.; Zeng, S. Q. *Nanoscale* **2011**, *3*, 2175−2181.

(14) Yu, M. X.; Li, F. Y.; Chen, Z. G.; Hu, H.; Zhan, C.; Yang, H.; Huang, C. H. *Anal. Chem.* **2009**, *81*, 930−935.

(15) Mai, H. X.; Zhang, Y. W.; Sun, L. D.; Yan, C. H. *J. Phys. Chem. C* **2007**, *111*, 13721−13729.

(16) Yang, D. M.; Li, C. X.; Li, G. G.; Shang, M. M.; Kang, X. J.; Lin, J. *J. Mater. Chem.* **2011**, *21*, 5923−5927.

(17) Shi, F.; Wang, J. S.; Zhang, D. S.; Qin, G. S.; Qin, W. P. *J. Mater. Chem.* **2011**, *21*, 13413−13421.

(18) Liu, Q.; Sun, Y.; Yang, T. S.; Feng, W.; Li, C. G.; Li, F. Y. *J. Am. Chem. Soc.* **2011**, *133*, 17122−17125.

(19) Boyer, J. C.; van Veggel, F. C. J. M. *Nanoscale* **2010**, *2*, 1417−1419.

(20) Tian, G.; Gu, Z. J.; Zhou, L. J.; Yin, W. Y.; Liu, X. X.; Yan, L.; Jin, S.; Ren, W. L.; Xing, G. M.; Li, S. J.; Zhao, Y. L. *Adv. Mater.* **2012**, *24*, 1226−1231.

(21) Lei, L.; Chen, D. Q.; Huang, P.; Xu, J.; Zhang, R.; Wang, Y. S. *Nanoscale* **2013**, *5*, 11298−11305.

(22) Huang, Q. M.; Yu, J. C.; Ma, E.; Lin, K. M. *J. Phys. Chem. C* **2010**, *114*, 4719−4724.

(23) Xiang, G. T.; Zhang, J. H.; Hao, Z. D.; Zhang, X.; Luo, Y. S.; Lü, S. Z.; Zhao, H. F. *CrystEngComm* **2014**, *16*, 2499−2507.

(24) Johnson, N. J. J.; Korinek, A.; Dong, C. H.; van Veggel, F. C. J. M. *J. Am. Chem. Soc.* **2012**, *134*, 11068−11071.

(25) Wang, Y.; Liu, K.; Liu, X. M.; Dohnalová, K.; Gregorkiewicz, T.; Kong, X. G.; Aalders, M. C. G.; Buma, W. J.; Zhang, H. *J. Phys. Chem. Lett.* **2011**, *2*, 2083−2088.

(26) Su, Q. Q.; Han, S. Y.; Xie, X. J.; Zhu, H. M.; Chen, H. Y.; Chen, C. K.; Liu, R. S.; Chen, X. Y.; Wang, F.; Liu, X. G. *J. Am. Chem. Soc.* **2012**, *134*, 20849−20857.

(27) Abel, K. A.; Boyer, J. C.; Andrei, C. M.; van Veggel, F. C. J. M. *J. Phys. Chem. Lett.* **2011**, *2*, 185−189.

(28) Li, X. M.; Shen, D. K.; Yang, J. P.; Yao, C.; Che, R. C.; Zhang, F.; Zhao, D. Y. *Chem. Mater.* **2013**, *25*, 106−112.

(29) Dong, C. H.; Korinek, A.; Blasiak, B.; Tomanek, B.; van Veggel, F. C. J. M. *Chem. Mater.* **2012**, *24*, 1297−1305.

(30) Zhang, F.; Che, R. C.; Li, X. M.; Yao, C.; Yang, J. P.; Shen, D. K.; Hu, P.; Li, W.; Zhao, D. Y. *Nano Lett.* **2012**, *12*, 2852−2858.

(31) Li, Z. Q.; Zhang, Y. *Nanotechnology* **2008**, *19*, 345606.

(32) Wei, Y.; Lu, F. Q.; Zhang, X. R.; Chen, D. P. *Chem. Mater.* **2006**, *18*, 5733−5737.

(33) Krämer, K. W.; Biner, D.; Frei, G.; Güdel, H. U.; Hehlen, M. P.; Lüthi, S. R. *Chem. Mater.* **2004**, *16*, 1244−1251.

(34) van der Ziel, J. P.; Van Uitert, L. G.; Grodkiewicz, W. H. *J. Appl. Phys.* **1970**, *41*, 3308−3315.

(35) Anderson, R. B.; Smith, S. J.; May, P. S.; Berry, M. T. *J. Phys. Chem. Lett.* **2014**, *5*, 36−42.

(36) Sommerdijk, J. L.; Bril, A. *Luminescence of Crystals, Molecules and Solutions*; Plenum Press: New York, 1973.

(37) Zhang, J. H.; Hao, Z. D.; Li, J.; Zhang, X.; Luo, Y. S.; Pan, G. H. *Light: Sci. Appl.* **2015**, *4*, e239.

(38) Lei, L.; Chen, D. Q.; Zhu, W. J.; Xu, J.; Wang, Y. S. *Chem.—Asian J.* **2014**, *9*, 2765−2770.